Dynamic compression of an Fe–Cr–Ni alloy to 80 GPa

Thomas S. Duffy[a)]
Department of Geosciences, Princeton University, Princeton, New Jersey 08544

Thomas J. Ahrens
Lindhurst Laboratory of Experimental Geophysics, Seismological Laboratory, California Institute of Technology, Pasadena, California 91125

(Received 15 May 1997; accepted for publication 29 July 1997)

Wave profiles were measured in an Fe–Cr–Ni alloy (stainless steel 304) shock compressed to Hugoniot stresses between 7 and 80 GPa. A single-stage propellant gun was used to generate shock states and time histories were recorded by velocity interferometry. The particle velocity measurements are generally consistent with impedance match calculations to ±2%. Unloading wave velocities were obtained from analysis of the release wave profiles. Using Eulerian finite strain theory and under the assumption of fully elastic initial release, the first and second pressure derivatives of the longitudinal modulus are given by: 7.9(0.5) and −0.16(0.06) GPa^{-1}, where the numbers in parentheses are one standard deviation uncertainties. The first and second pressure derivatives of the adiabatic bulk modulus are: 6.4(1.0) and −0.17(0.08) GPa^{-1}. The unloading wave velocities are generally consistent with extrapolated trends from low-pressure ultrasonic data as well as with higher stress shock measurements on an alloy of similar composition. From 1 bar to 80 GPa, Poisson's ratio, ν, increases with Hugoniot stress, σ (in GPa), according to the relation: $\nu=0.29+0.0008\sigma$. The Hugoniot elastic limit of 304 steel was found to be 0.35(0.12) GPa, and the initial yield stress is 0.21(0.07) GPa. The elastic precursor velocity was 5.8(0.1) km/s. Numerical simulations of the wave profiles using a constitutive model that incorporates a Bauschinger effect and stress relaxation reproduced the main features observed in the profiles. Release adiabats were also calculated from the measured wave profiles. The shear stress at unloading was determined to vary with stress according to the relation: $\tau_0+\tau_c=0.149+0.018\sigma$, where σ is given in GPa.
 [S0021-8979(97)05921-5]

I. INTRODUCTION

The elastic properties of Fe and Fe alloys at high pressure are important for understanding the seismic properties of the Earth's core. While the core is known to be dominantly iron on the basis of density data and cosmochemical arguments, a number of possible alloying elements have been proposed. Measurement of elastic wave velocities in iron alloys offers a means to place constraints on the nature and amount of such components. Comparing laboratory data to seismic data under core conditions requires large and uncertain extrapolations in pressure and temperature. It is therefore important to delineate the separate pressure and temperature variation of wave velocities.

In this study, wave profiles are reported for an Fe–Cr–Ni alloy (304 stainless steel) shock compressed to 80 GPa. Elastic properties were determined from the interface particle velocity histories measured using velocity interferometry. Comparison of wave profile measurements to finite difference simulations provides information on constitutive properties such as the yield stress, the shear stress change upon unloading, and the Bauschinger effect. These properties provide insights into the details of the shock-compression process, an understanding of which is necessary to relate shock data to static data or geophysical measurements of the Earth's interior. Stainless steel 304 has been the subject of a number of shock-compression studies. The Hugoniot equation of state (EOS) has been determined to 190 GPa,[1] and shock temperatures have been measured between 138 and 271 GPa.[2,3]

II. EXPERIMENTAL TECHNIQUE

A. Samples

The chemical composition of the Fe–Cr–Ni alloy was determined by electron microprobe analysis and is listed in Table I together with the compositions reported in other studies using this material. Samples were machined into 32-mm-diam disks from commercial steel rods. The end faces were lapped flat and parallel to better than 0.01 mm. Bulk and crystal densities were measured by weighing the samples in air and toluene under controlled temperature conditions. The average crystal density was 7.88 ± 0.01 g/cm^3, in good agreement with the x-ray density of 7.89 g/cm^3. The average bulk density was 7.87±0.01 g/cm^3, indicating minimal porosity. The longitudinal sound velocity was measured ultrasonically and found to be 5.75±0.03 km/s, in agreement with a previous value of 5.76±0.02 km/s.[4] The rear surface of each specimen was lapped to either a diffuse or specularly reflecting surface.

B. Experiments

1. Dynamic loading system

The samples were shock-loaded using a 40 mm bore propellant gun. The experimental apparatus for achieving

a)Electronic mail: duffy@geo.princeton.edu

TABLE I. Chemical composition of stainless steel 304 samples in weight percentages. The analysis of the samples used in this study was via JEOL Superprobe.

Element	This study	Ref. 1	Ref. 2
Fe	69.7	68	69.3
Cr	19.3	19	19.4
Ni	8.2	10	9.1
Mn	1.3	2	-
Si	0.4	1	0.7
Total	98.9	100	98.5

one-dimensional planar shock loading has been described in detail elsewhere.[5,6] A brief summary is included here. Projectiles are ~100 g and consist of a lexan sabot with a variable thickness, 32-mm-diam flyer plate, backed by a ~3-mm-thick layer of 40 lb/ft^3 polyurethane foam. The flyer plate materials used in this study were polymethyl methacrylate (PMMA), 304 stainless steel, and tantalum. The equation of state properties of the flyers, as well as those of other materials used in these experiments, are listed in Table II. Variable amounts of nitroglycerine-nitrocellulose propellant are used to accelerate the projectile down the 8 m length of the gun barrel into an evacuated chamber containing the target assembly. Impact velocities between 0.9 and 2.5 km/s are achievable in this manner. Projectile velocity is determined to ~1%–2% precision using both double-exposure flash x-ray photography and time-interval counters triggered by laser-beam interrupts.

2. Interferometry

The diagnostic technique used in this study was velocity interferometry, which gives a time history of the motion of a diffusely or specularly reflecting sample surface. Two types of interferometers were used: the specular velocity interferometer (SVI)[11] and the velocity interferometer system for any reflector (VISAR)[12]. Both interferometers work on the same principle: motion of the target surface induces a Doppler shift in reflected laser light, which creates interference fringes in a modified Michelson interferometer. In the SVI, a delay time is introduced by routing a portion of reflected light through a long delay leg. To produce fringes in the recombined beam, it is necessary that the sample retain a mirror finish after shock wave passage. For this reason, SVI experiments were limited to stresses below 12 GPa.

TABLE II. Equation of state standards. Numbers in parentheses are one standard deviation uncertainties. ρ_0 is the density, c_0 and s are shock wave EOS constants, γ_0 is the Grüneisen parameter, ν_0 is Poisson's ratio, and Y_0 is the yield strength.

Material	ρ_0 (bulk) (g/cm^3)	c_0 (km/s)	s	γ_0	ν_0	Y_0 (GPa)	References
304 Steel	7.87(2)	4.58(1)	1.49(1)	2.2	0.29	0.2	a,b
PMMA	1.18(1)	2.58(2)	1.53(1)	1.0	-	-	c
Al6061	2.683(3)	5.349(56)	1.338(20)	2.1	0.34	0.2	c
Al2024	2.784(5)	5.33(5)	1.34(2)	2.0	-	-	c
Ta	16.65(3)	3.293(5)	1.307(25)	1.6	0.34	0.8	d
LiF	2.64(2)	5.15(3)	1.35(1)	1.6	0.22	0.2	c
Al_2O_3	3.985(5)	11.19(1)	1.00(5)	1.3	-	-	e
Lexan	1.193(1)	2.421(33)	1.32(11)	-	-	-	c
Foam	0.64(1)	0.87	2.03	-	-	-	f

[a]This study.
[b]Reference 1.
[c]Reference 7.
[d]Reference 8.
[e]Reference 9.
[f]Reference 10.

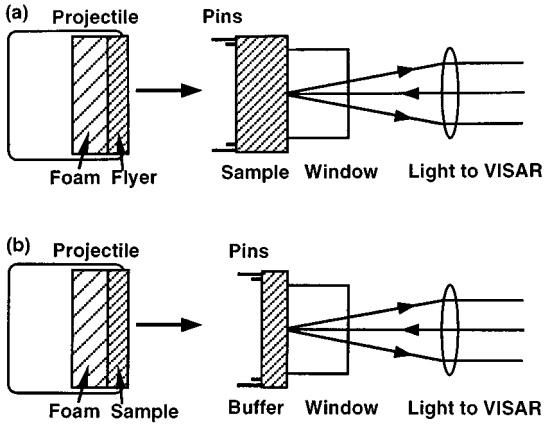

FIG. 1. (a) Forward- and (b) reverse-impact arrangement for velocity interferometer experiments.

In the VISAR, a small time delay (1–2 ns) is introduced in one leg of the interferometer by means of fused silica cylinders, but the interferometer mirrors are positioned such that the distance along both paths appears to be the same from the point of view of the detector. This allows interference fringes to be formed with a spatially incoherent source. The VISAR we have constructed is similar to that originally described by Ref. 12 except that it incorporates the push-pull modification and data reduction scheme of Ref. 13.

For both the VISAR and SVI, the relationship between surface velocity and the number of interference fringes can be expressed as[12]

$$u(t-\tau/2)=kF(t), \tag{1}$$

where u is the surface velocity, t is time, τ is the delay time of the interferometer, k is the velocity per fringe constant, and F is number of fringes recorded. For the VISAR, the fringe constant k is given by

$$k=\frac{\lambda}{2\tau w_c e_c}, \tag{2}$$

where λ is the laser wavelength, τ is the delay time of the interferometer which depends on the length of étalon material and its refractive index, w_c is a correction term that accounts for the stress-induced change of refractive index in the shock-compressed window, and e_c is a correction term that accounts for dispersion in the fused silica étalons. The time resolution of our VISAR is estimated to be 2–3 ns.

3. Target assembly

Two types of target assemblies were used in the present experiments. In the forward-impact geometry [Fig. 1(a)], the Fe–Cr–Ni sample is impacted with a flyer plate of PMMA, 304 steel, or tantalum. An array of 4–6 electrical shorting

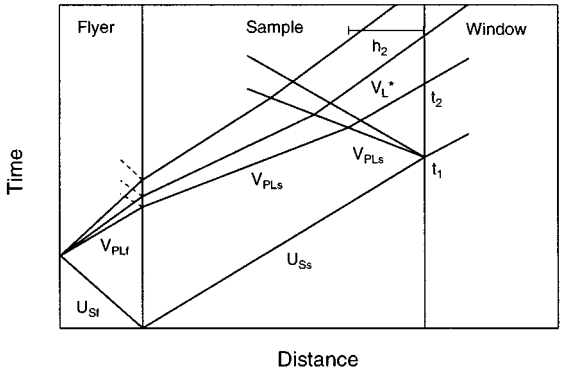

FIG. 2. Lagrangian x-t diagram for forward-impact experiments. U_{Ss} and U_{Sf} are the shock wave velocities in the sample and flyer, respectively. V_{PLs} and V_{PLf} are the Lagrangian velocities of initial release in the sample and flyer, respectively. V_L^* is the sound speed in the interaction region (h_2) defined by the intersection of the forward and backward leading characteristics. t_1 is the arrival time of the plastic wave at the interface monitored by the VISAR. t_2 marks the onset of the unloading history at the interface.

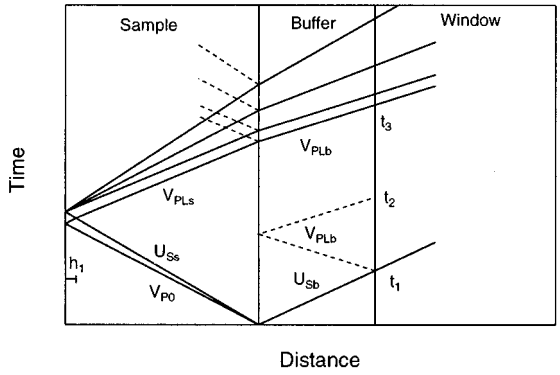

FIG. 3. Lagrangian x-t diagram for reverse-impact experiments. The subscript b refers to the buffer, and the subscript s refers to the sample. V_{P0} is the elastic precursor velocity in the sample. t_1 is the arrival time of the plastic wave at the interface. At t_2, a weak reverberation in the buffer is detected. t_3 marks the onset of the unloading history at the interface. Other symbols are the same as in Fig. 2.

pins are used to trigger the recording instrumentation and to measure the tilt between the flyer and target at impact, which was typically a few milliradians. A Z-cut sapphire or lithium fluoride window is affixed to the rear surface of the target, using a $\sim$10-μm-thick epoxy layer.

Sapphire provides an excellent impedance match to 304 stainless steel but was not used above 12 GPa because its yielding properties preclude its use as an interferometer window at higher stresses[9]. LiF, which has been calibrated for use as a VISAR window to 115 GPa[14], was used for the majority of the present experiments, although its impedance differs from steel by more than a factor of 2.

The main features of a forward-impact VISAR experiment are shown in the Lagrangian distance-time diagram of Fig. 2. Impact generates shocks propagating into the flyer and sample, which, depending on stress level and material properties, could be preceded by an elastic precursor. Upon arriving at the interface between the flyer and its foam backing, the shock wave reflects as a rarefaction fan[15], partially unloading the material from its high-stress state. The rarefaction fan is shown as a set of characteristics representing initial elastic, plastic, and final unloading. When the flyer and sample are different materials, the characteristics will be bent when encountering the change in material properties at the flyer-sample interface. The shock traveling through the sample reaches the sample-window interface at time t_1 and is recorded by the VISAR. Because of the mechanical impedance mismatch at this interface, a partial rarefaction is generated, which propagates back into the sample, interacts with the oncoming rarefaction, and perturbs the unloading wave form observed at the sample-window interface beginning at time t_2.

The effect of this wave interaction is eliminated in the reverse-impact geometry. In this case, the sample is mounted in the projectile and used to impact a thin (1–2 mm) aluminum buffer with an LiF window epoxied to it [Fig. 1(b)]. As shown in Fig. 3, impact at $t=0$ produces compressive waves in both the buffer and sample. The arrival of the shock at the buffer-window interface produces only a small perturbation, as the impedances of aluminum and LiF differ by only about 5%. A weak rarefaction is propagated back through the buffer, which returns to the interface as a weak reshock at time t_2. The compressive-wave structure in the sample reflects from the sample-foam interface and a rarefaction fan propagates back through the sample and buffer as shown, with the first arrival reaching the interface at t_3. The distortion of the wave form is minimal in this geometry. However, the maximum stress attainable for a given velocity is limited by the low impedance of the aluminum buffer.

In both geometries, sample dimensions are chosen to maintain uniaxial strain conditions throughout the unloading of the specimen. The window thickness is also chosen so that the shock arrives at the LiF free surface after the arrival of the elastic and plastic waves at the buffer-window or sample-window interface. The experimental conditions for the forward-geometry SVI experiments and both the forward- and reverse-impact VISAR experiments are listed in Tables III, IV, and V.

III. RESULTS

Interface particle velocity histories for the VISAR experiments are shown in Fig. 4. The results of experiments 804 and 802 have been scaled by factors of 1.12 and 1.07, respectively, to account for non-normal incidence of the laser beam for these two experiments and to bring them into accord with the impedance-match results discussed below.

TABLE III. Initial conditions for SVI experiments. u_{fp} is the impact velocity.

	Flyer			Sample		Window
Shot	Material	Thickness (mm)	u_{fp} (km/s)	ρ_0 (g/cm^3)	Thickness (mm)	Material
746	PMMA	0.993(2)	1.62(2)	7.857(16)	2.004(4)	Sapphire
747	PMMA	0.983(6)	1.37(1)	7.838(12)	2.075(3)	Sapphire
749	PMMA	1.575(6)	1.79(1)	7.857(8)	6.429(4)	Sapphire
771	PMMA	2.159(3)	2.15(3)	7.820(9)	6.300(4)	LiF

TABLE IV. Initial conditions for forward-impact VISAR experiments.

	Flyer				Sample		Window	
Shot	Material	ρ_0 (g/cm^3)	Thickness (mm)	u_{fp} (km/s)	ρ_0 (g/cm^3)	Thickness (mm)	ρ_0 (g/cm^3)	Thickness (mm)
802	ss304	7.875(12)	2.613(5)	1.15(2)	7.878(6)	6.299(4)	2.63(1)	7.953(2)
804	ss304	7.88(2)	2.548(4)	1.94(12)	7.847(11)	6.352(9)	2.63(1)	7.945(5)
809	Ta	16.47(4)	1.858(5)	2.00(4)	7.835(12)	6.375(1)	2.632(1)	7.950(2)
812	Ta	16.61(2)	1.892(1)	2.46(4)	7.827(23)	6.359(2)	2.626(1)	7.827(2)
813	ss304	7.882(2)	2.027(4)	1.19(2)	7.867(6)	6.415(2)	2.625(5)	7.831(1)
847	Ta	16.57(3)	1.891(3)	2.45(3)	7.891(6)	6.335(3)	2.630(2)	8.128(7)
862	Ta	16.55(3)	2.275(3)	2.52(4)	7.893(6)	6.326(4)	2.632(2)	8.150(4)

The forward-impact experiments are characterized by a shock arrival, followed by a flat-topped plateau region, and by broad, featureless unloading. The shape of the wave profile changes little with increasing stress. The scalloping observed for experiment 812 is an artifact of data reduction due to severe changes in sample reflectivity during this experiment. The reverse-impact experiments show a slight dip in particle velocity in the plateau region because of the arrival of the reverberation through the aluminum buffer. The initial unloading is more distinct in the reverse impacts.

The measured impact velocity, together with EOS data (Table II), can be used to determine the Hugoniot state through impedance matching[6]. By requiring the stress to be continuous across the impact interface, the particle velocity, u_p, is constrained by the known stress-particle velocity relations in the flyer and target. The shock velocity, U_S, is then determined from the material law:

$$U_S = c_0 + s u_p . \tag{3}$$

In the case of reflection from a higher or lower impedance boundary, the release isentrope is approximated by using the Hugoniot itself, and the free-surface approximation is made.[16] The resulting Hugoniot states for the samples are listed in Tables VI and VII together with the calculated and measured particle velocities at the sample-window interface. In most cases, the calculated particle velocities agree with the VISAR measurements within $\pm 2\%$. The measured particle velocities lie systematically below the impedance-match calculations, however.

Unloading wave velocities were determined from the initial unloading points using the analysis outlined below. For the SVI experiments, the initial unloading point was measured directly from the interferometer records, and the wave profiles were not analyzed in detail. For VISAR experiments 804 and 847, only the initial portions of the unloading history were recovered because of recording failures. These give well-defined initial unloading velocities but no additional information.

For experiments using the reverse geometry, the following expression for the initial Lagrangian unloading velocity, V_{PLs}, can be obtained with reference to Fig. 3:[17]

$$V_{PLs} = \frac{x_s - h_1}{\Delta t + x_b/U_{Sb} - (x_s + h_1)/V_{P0s} - x_b/V_{PLb}}, \tag{4}$$

where x_s and x_b are the sample and buffer thicknesses, U_{Sb} and V_{PLb} are the shock and unloading wave velocities in the buffer, $\Delta t = t_3 - t_1$ is the time between the shock arrival at the reflector and the initial arrival of the unloading wave, h_1 is the thickness of the interaction region between the precursor and shock at the rear of the sample:

$$h_1 = x_s \left(\frac{V_{P0s} - U_{Ss}}{V_{P0s} + U_{Ss}} \right), \tag{5}$$

where $h_1 = 0$ if $U_{Ss} > V_{P0s}$. The elastic precursor velocity was taken to be 5.76 ± 0.02 km/s from ultrasonic compressional sound velocity measurements[4]. The shock velocities in the flyer and sample are determined from impedance matching (Tables VI and VII). The unloading velocity in the buffer is obtained from the reverberation arrival time:

$$V_{PLb} = \frac{2x_b}{t_2 - t_1}, \tag{6}$$

which makes use of the experimental observation that release waves and reshocks in aluminum travel with the same velocity[18]. In addition, the slight change in stress state ($\sim 3\%$) caused by the reverberation is neglected, and it is assumed that the material can support passage of multiple

TABLE V. Initial conditions for reverse impact VISAR experiments.

	Sample			Buffer			Window	
Shot	ρ_0 (g/cm^3)	Thickness (mm)	u_{fp} (km/s)	Material	ρ_0 (g/cm^3)	Thickness (mm)	ρ_0 (g/cm^3)	Thickness (mm)
820	7.887(12)	3.192(5)	1.95(3)	Al2024	2.720(20)	0.809(2)	2.625(10)	11.930(2)
849	7.855(4)	3.189(2)	2.31(4)	Al6061	2.682(4)	1.970(1)	2.631(2)	12.118(4)
858	7.871(11)	3.192(4)	1.29(2)	Al6061	2.681(4)	1.938(3)	2.630(2)	12.121(4)

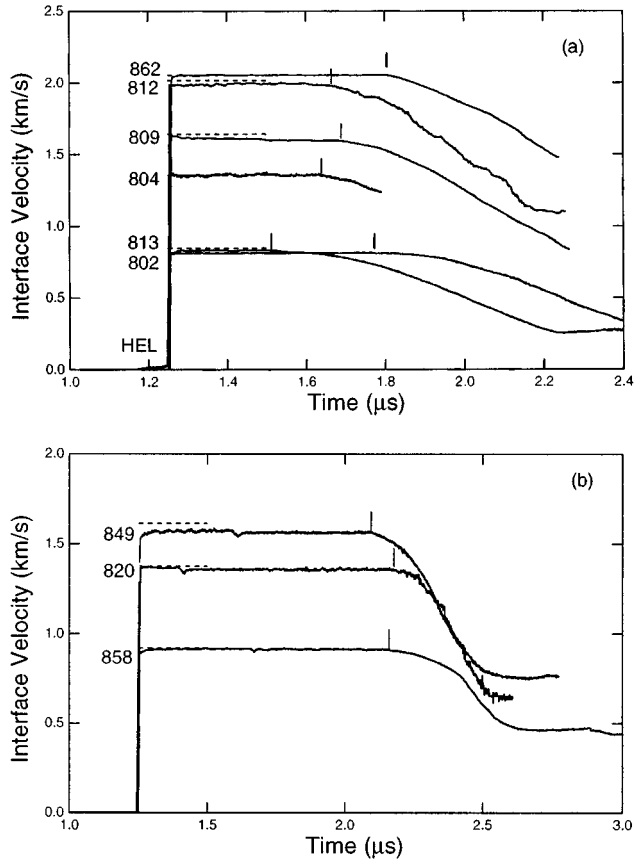

FIG. 4. Interface wave profiles for (a) forward- and (b) reverse-impact experiments. Shot numbers are listed to the left of each wave profile. Dashed lines show the particle velocity expected on the basis of impedance-matching calculations. The vertical lines show the initial unloading. The times are relative to an arbitrary trigger signal.

elastic waves. Unloading wave velocities in aluminum are discussed in Ref. 17. Lagrangian and Eulerian wave velocities are related through

$$V_{PL}=\frac{\rho}{\rho_0}V_P. \tag{7}$$

Interpretation of the forward-impact experiments is complicated by the wave interaction that occurs in the sample interior. In this case (Fig. 2) the velocity is expressed as

$$V_{PLs}=\frac{a-h_1-h_2}{t_2-h_2/V_L^*-(x_f+h_1)/U_{1f}-b}, \tag{8}$$

where x_f is the flyer thickness, U_{1f} is the velocity of the initial loading wave (shock or precursor) in the flyer, and h_1 is given by

TABLE VI. Forward-impact impedance-match solutions. u_{pc} is the calculated interface particle velocity, and u_{pm} is the measured interface particle velocity.

	Sample				Sample/Window	
Shot	u_p (km/s)	U_s (km/s)	ρ (g/cm^3)	σ (GPa)	u_{pc} (km/s)	u_{pm} (km/s)
746	0.209(5)	4.891(11)	8.208(19)	8.1(2)	0.192(6)	-
747	0.170(3)	4.834(11)	8.119(13)	6.5(1)	0.156(4)	-
749	0.239(4)	4.936(12)	8.257(11)	9.3(1)	0.221(5)	-
771	0.288(12)	5.010(21)	8.298(24)	11.3(5)	0.412(22)	-
802	0.575(8)	5.437(16)	8.810(13)	24.6(4)	0.814(11)	0.758
804	0.970(6)	6.025(90)	9.385(86)	46.0(3.6)	1.357(82)	1.220
809	1.183(24)	6.342(38)	9.630(35)	58.7(1.5)	1.644(32)	1.611
812	1.458(22)	6.753(37)	9.983(41)	77.1(1.6)	2.017(30)	1.991
813	0.597(8)	5.470(16)	8.831(13)	25.7(4)	0.847(10)	0.831
847	1.447(15)	6.736(27)	10.050(22)	76.9(1.1)	2.005(20)	-
862	1.485(21)	6.793(35)	10.102(30)	79.6(1.6)	2.056(29)	2.054

$$h_1=x_f\left(\frac{V_{0f}-U_{Sf}}{V_{0f}+U_{Sf}}\right), \tag{9}$$

and $h_1=0$ if $U_{Sf}\geqslant V_{0f}$. For symmetric impact, $a=x_f+x_s$ and $b=0$. For a non-symmetric impact, $a=x_s$ and $b=(x_f-h_1)/V_{PLf}$, where V_{PLf} is the Lagrangian unloading velocity in the flyer. The arrival time t_2 is given by either

$$t_2=\Delta t_{SR}+\frac{x_s}{U_{Ss}}, \tag{10}$$

or

$$t_2=\Delta t_{PR}+\frac{x_s}{V_{P0s}}, \tag{11}$$

where Δt_{SR} is the time difference between the shock and release arrivals and Δt_{PR} is the time difference between the elastic precursor and release arrivals.

The interaction region h_2 is defined by the point where the forward-traveling and backward-traveling rarefactions intersect:

$$h_2=\frac{V_{PLs}}{2}\left[x_f\left(\frac{1}{V_{PLf}}+\frac{1}{U_{1f}}\right)+x_s\left(\frac{1}{V_{PLs}}-\frac{1}{U_{Ss}}\right)+h_1\left(\frac{1}{U_{1f}}-\frac{1}{V_{PLf}}\right)\right]. \tag{12}$$

The average velocity in the interaction region, V_L^*, was taken to be the bulk Lagrangian velocity at the interaction-region stress. The bulk velocity is appropriate because of the large stress change in the interaction region and the low yield

TABLE VII. Reverse-impact impedance-match solutions.

	Sample				Buffer			Buffer/Window	
Shot	u_p (km/s)	U_s (km/s)	σ (GPa)	ρ (g/cm^3)	u_p (km/s)	U_s (km/s)	ρ (g/cm^3)	u_{pc} (km/s)	u_{pm} (km/s)
820	0.604(10)	5.477(39)	26.1(6)	8.863(21)	1.344(21)	7.132(26)	3.519(26)	1.376(22)	1.370
849	0.718(13)	5.649(24)	31.8(8)	8.998(20)	1.558(18)	7.474(69)	3.406(15)	1.615(27)	1.570
858	0.390(6)	5.160(15)	15.8(3)	8.514(15)	0.900(13)	6.554(58)	3.108(9)	0.919(13)	0.914

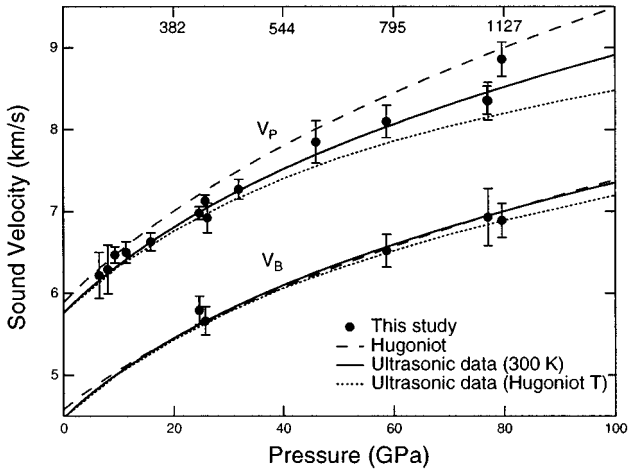

FIG. 5. Measured compressional (V_P) and bulk (V_B) wave velocities in the Fe–Cr–Ni alloy. Also shown are bulk and compressional velocities calculated from the Hugoniot slope, using the assumptions that $\rho\gamma$ and Poisson's ratio are constant (dashed lines). The solid curves are third-order finite-strain extrapolations of 1 GPa ultrasonic data (see Ref. 24). The dotted curves have been corrected for thermal differences between the Hugoniot and the isotherm. The numbers in parentheses near the top are estimated shock temperatures in K at 20 GPa intervals. The difference between the Hugoniot stress and hydrostatic pressure has been neglected here.

strength of 304 steel. Estimates of the bulk wave velocity were obtained from Hugoniot slope calculations described below and agree with measured bulk velocities discussed below.

Equations (8) and (12) form a coupled set that are solved iteratively. The interaction region, h_2, typically extends about 1/4 of the distance into the sample. Neglect of the interaction region would produce about a 5% decrease in the measured velocities. For the flyer plates, compressional unloading velocities were estimated by extrapolating trends based on available data for Ta[19,20] and PMMA[9,21] together with ambient-pressure ultrasonic data. For Ta, the following relationship between Eulerian unloading velocity (in km/s) and shock stress (in GPa) was used:[22]

$$\ln V_P = 1.4298 - 0.0263 \ln \sigma + 0.0205 \ln^2 \sigma. \tag{13}$$

In the case of PMMA, a quadratic relation between Lagrangian unloading velocity and the particle velocity was used:

$$V_{PL} = 2.86 + 4.04 u_p + 0.42 u_p^2. \tag{14}$$

The measured Hugoniot sound velocities are shown as a function of pressure in Fig. 5 and listed in Table VIII. Velocities obtained using the two types of experimental geometries are in good agreement, suggesting that our corrections for the interaction region are adequate. Velocities obtained using the SVI and the VISAR are also consistent with each other.

IV. DISCUSSION

A. Sound velocities

For a solid, the initial unloading velocity of a shocked material corresponds to an elastic or quasi-elastic wave velocity,[15,23] while for a liquid it corresponds to the bulk velocity, V_B. The initial velocities we have measured lie significantly above expected bulk velocities, consistent with the expectation that Fe–Cr–Ni remains solid over the stress range investigated.

TABLE VIII. Measured unloading wave velocities in Fe–Cr–Ni alloy. V_B is the bulk sound velocity and ν is Poisson's ratio.

Shot	Stress (GPa)	V_P (km/s)	V_B (km/s)	$\rho\gamma$ (g/cm^3)	ν
747	6.5	6.22 (0.28)	-	-	0.30 (0.04)
746	8.1	6.29 (0.30)	-	-	0.30 (0.04)
749	9.3	6.47 (0.10)	-	-	0.29 (0.01)
771	11.3	6.50 (0.13)	-	-	0.30 (0.02)
858	15.8	6.63 (0.11)	-	-	0.31 (0.01)
802	24.6	6.98 (0.08)	5.79 (0.17)	−15 (33)	0.33 (0.01)
813	25.7	7.13 (0.07)	5.66 (0.17)	14 (31)	0.31 (0.01)
820	26.1	6.92 (0.18)	-	-	0.34 (0.02)
849	31.8	7.27 (0.12)	-	-	0.32 (0.02)
804	46.0	7.85 (0.26)	-	-	0.31 (0.03)
809	58.7	8.10 (0.20)	6.52 (0.20)	16 (12)	0.32 (0.02)
847	76.9	8.36 (0.17)	-	-	0.35 (0.02)
812	77.1	8.35 (0.23)	6.93 (0.35)	16 (14)	0.35 (0.03)
862	79.6	8.86 (0.21)	6.89 (0.21)	22 (8)	0.30 (0.02)

Bulk wave velocities were obtained from detailed analysis of the unloading profiles discussed below. The measured velocities are compared with extrapolations of low-pressure ultrasonic data in Fig. 5. Extrapolations were performed using third-order finite strain theory,[22,25] and pressure derivatives were taken from measurements to 1 GPa.[24] The compressional and bulk velocities are in good agreement with ultrasonic extrapolations throughout the stress range of this study. The initial unloading velocities in fcc metals might be lower than ultrasonic measurements due to quasielastic release[23] and due to higher temperatures along the Hugoniot state. Temperature calculations indicate that the Hugoniot temperature at 80 GPa is 854 °C.[1] The temperature coefficients of compressional, V_P, and bulk velocity, V_B, are given by

$$\left(\frac{\partial V_P}{\partial T}\right)_P = \frac{V_P}{2}[(\partial C_L/\partial T)_P/C_L + \alpha], \tag{15}$$

$$\left(\frac{\partial V_B}{\partial T}\right)_P = \frac{V_B}{2}[(\partial K_S/\partial T)_P/K_S + \alpha], \tag{16}$$

where T is the temperature, $C_L = K_S + 4G/3$ is the longitudinal modulus, K_S is the bulk modulus, G is the shear modulus, and α is the thermal expansivity. We assume that the temperature coefficients of the elastic moduli as well as the product αK_s are constant with stress. The temperature coefficients of the elastic moduli for 304 steel were taken from Ref. 26. From Eqs. (15) and (16) we find that $(\partial V_P/\partial T)_P$ increases from -7×10^{-4} km/s/K at ambient pressure to -3.5×10^{-4} km/s/K at 80 GPa, while $(\partial V_B/\partial T)_P$ increases from -2.64×10^{-4} to -1.21×10^{-4} km/s/K over the same stress range. The resultant thermal corrections to the 300 K velocities are shown in Fig. 5. The measured Hugoniot velocities lie above the calculated values, suggesting that thermal effects may be smaller than those inferred here or that extrapolation of low-pressure ultrasonic data may not be reliable.

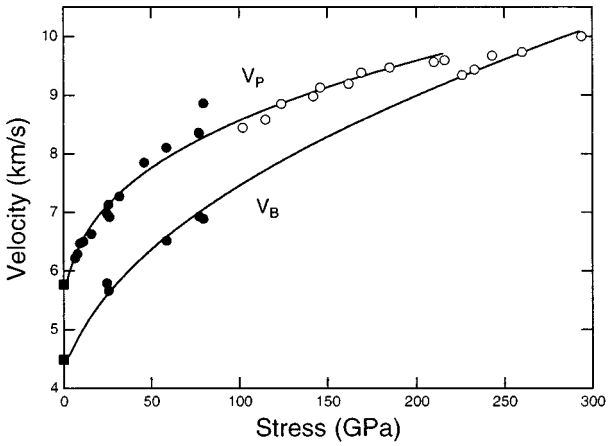

FIG. 6. Sound velocities in Fe–Cr–Ni alloys to 300 GPa. Filled circles are this study (304 steel); open circles are data of Ref. 27 (316 steel). Filled squares are ambient pressure data (see Ref. 24). Solid curves are fits to compressional and bulk velocity.

Sound velocity measurements in an Fe–Cr–Ni alloy of similar composition (steel 316) have also been reported at shock stresses between about 100 and 300 GPa[27]. Figure 6 shows that the two data sets are generally consistent, although it appears that the trend of the compressional velocities measured here may be slightly higher than the measurements of Ref. 27. The variation of Hugoniot compressional sound velocity with stress in Fe–Cr–Ni alloy to 220 GPa can be described by (Fig. 6)

$$\ln V_P = 1.742 + 0.024 \ln \sigma + 0.014 \ln^2 \sigma. \tag{17}$$

Similarly, the variation in bulk sound velocity along the Hugoniot from ambient pressure to nearly 300 GPa is given by

$$\ln V_P = 1.519 - 0.036 \ln \sigma + 0.031 \ln^2 \sigma. \tag{18}$$

The bulk sound velocity along the Hugoniot can be obtained by relating the initial slope of the release adiabat to the Hugoniot through the Mie–Grüneisen equation.[1] This can be expressed as

$$V_B = \sqrt{\frac{K_S}{\rho}} = \left\{ \left(\frac{\partial \sigma}{\partial \rho} \right)_H \left[1 - \left(\frac{1}{\rho_0} - \frac{1}{\rho} \right) \frac{\rho \gamma}{2} \right] + \frac{\sigma \gamma}{2\rho} \right\}^{1/2}, \tag{19}$$

where $(\partial \sigma / \partial \rho)_H$ is the local Hugoniot slope, and γ is the Grüneisen constant. Bulk sound velocities calculated in this manner for 304 steel are shown in Fig. 5, where the assumption has been made that $\gamma \rho$ is constant. Also shown in the figure is the compressional velocity calculated by making the additional assumption that Poisson's ratio is a constant function of stress. That this assumption overpredicts the data implies that Poisson's ratio increases with compression. The variation of Poisson's ratio along the Hugoniot to 80 GPa is given by (Table VIII):

$$\nu = 0.29(0.01) + 8(2) \times 10^{-4} \sigma, \tag{20}$$

where σ is given in GPa.

Measured bulk sound velocities can, in conjunction with the equation of state, be used to solve Eq. (19) for the product $\rho \gamma$. The results of this calculation are given in Table VIII. The uncertainties are quite large, particularly at low stress, and illustrate that a substantial range of Grüneisen parameters can fit the present data. For comparison, $\rho_0 \gamma_0 = 17$ at ambient pressure for 304 steel.[1]

TABLE IX. Comparison of elastic properties of Fe–Cr–Ni alloy under Hugoniot conditions (5–80 GPa) with ultrasonic measurements to 1 GPa.[a] Single and double primes represent first and second pressure derivatives of the elastic moduli, respectively.

Modulus	Hugoniot	Ultrasonics
C_{Lo} (GPa)	262 (2)	261.3
K_0 (GPa)	158 (1)	158.2
G_0 (GPa)	78 (2)	77.4
C'_{Lo}	7.9 (0.5)	7.90
K'_o	6.4 (1.0)	5.57
G'_o	1.1 (0.8)	1.75
C''_{Lo} (GPa^{-1})	−0.16 (0.06)	-
K''_o (GPa^{-1})	−0.17 (0.08)	-
G''_o (GPa^{-1})	0.0 (0.08)	-

[a]See Ref. 24.

Under the assumption that the release wave velocities are fully elastic, the data of Fig. 5 can be used to extract aggregate elastic constants. We use fourth order Eulerian finite strain expressions,[22,25] and the small difference between the Hugoniot longitudinal stress and the hydrostatic pressure has been ignored. A least-squares fit to the Hugoniot data and the ambient-pressure elastic moduli yield the elastic coefficients along the Hugoniot (Table IX). Both first and second pressure derivatives of the aggregate bulk and shear modulus are obtained. The first pressure derivatives are consistent with ultrasonic values within their uncertainties.

B. Constitutive response

As seen in Fig. 4(a), the elastic precursor was recorded in two experiments (802 and 813). The precursor manifests itself as a ramp increase in velocity with a distinct shoulder. The magnitude of the Hugoniot elastic limit (HEL) was determined from the measured particle velocity of the elastic wave at the shoulder, using

$$\sigma_{HEL} = \frac{(Z_s + Z_w) u_{pm}}{2}, \tag{21}$$

where σ_{HEL} is the elastic limit stress, u_{pm} is the measured interface particle velocity, and Z_s and Z_w are the impedances of the sample and window given by the product of density and elastic wave velocity. The measured particle velocities were 0.011 ± 0.005 km/s, and the corresponding HEL stress was 0.35 ± 0.12 GPa. The Hugoniot elastic limit of an Fe–Cr–Ni stainless steel of similar composition was determined to be 0.56 GPa at 293 K.[28] The yield stress Y_0 can be obtained from

$$Y_0 = \frac{(1 - 2\nu)}{(1 - \nu)} \sigma_{HEL}, \tag{22}$$

where ν is Poisson's ratio. The value of Y_0 obtained from these experiments is 0.21 ± 0.07 GPa, which is consistent with values of 0.2 and 0.34 GPa reported previously for this material[29,30].

The velocity of the elastic precursor was calculated to be 5.72 ± 0.1 km/s and 5.76 ± 0.1 km/s for the two experiments. This was determined by using the measured time difference between the precursor shoulder and the shock arrival, together with the shock velocity determined from the impedance-match solution. This is in excellent agreement with the ultrasonic value of 5.76 ± 0.03 km/s discussed above.

Numerical simulations of the wave profiles were carried out using the one-dimensional Lagrangian finite difference wavecode WONDY.[31] This wavecode solves equations for conservation of mass, momentum, and energy together with a constitutive law. Relevant geometric- and material-property data are input for each material layer in a particular experiment. The simplest material law for solids that retain their strength is the elastic-perfectly plastic (EPP) model.

Wavecode simulations of the experimental particle velocity histories were first performed by treating each material layer as EPP except for the foam layer for which the model of Ref. 10 was used. The wave forms predicted by this model were in poor agreement with the data. In an attempt to improve upon this, we broadened our constitutive model to include both a Bauschinger effect and strain rate dependent stress relaxation. The Bauschinger effect, or anisotropic strain hardening, is a consequence of the micromechanics of the deformation process and can be described as a hysteresis in the stress-strain curve. The yield stress upon loading and unloading differs and the clear distinction between elastic and plastic behavior is blurred by this effect. The Bauschinger effect is implemented into the code using a multi-element kinematic model which requires a set of normalized weighting factors, a_i and a set of elemental yield stresses Y_i[32].

The possibility for strain-rate dependent stress relaxation was also included. In this phenomenon, the deviatoric stresses temporarily exceed their equilibrium value and relax back to steady state at a rate controlled by a time constant. The viscoplastic response is incorporated into the wavecode using a Maxwellian relaxation function, g, of the form

$$g = \frac{\sigma' - \sigma'_{eq}}{G\tau}, \tag{23}$$

where σ' is the stress deviator, σ'_{eq} is the equilibrium stress deviator, G is the shear modulus, and τ is the effective material relaxation time. The stress deviators, together with the pressure, determine the axial stress, σ:

$$\sigma = P + \sigma', \tag{24}$$

where the pressure is determined using the Hugoniot EOS and the Mie–Grüneisen equation. The complete constitutive equation is described in Ref. 31.

The measured wave profiles were fit in an iterative fashion by adjusting the parameters of the Bauschinger model and the relaxation time constant. The LiF windows were treated as elastic-perfectly plastic as were the Ta flyer plates.

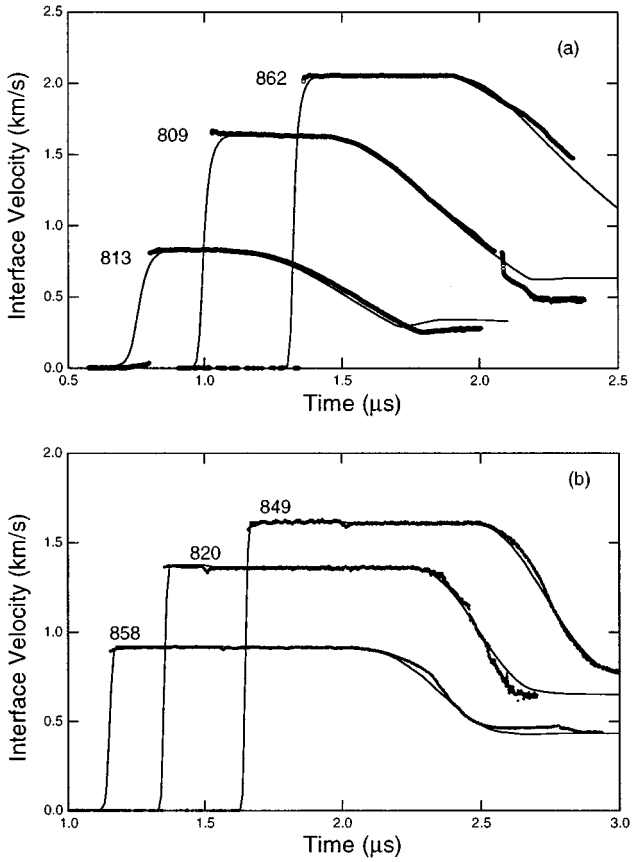

FIG. 7. Comparison of measured wave profiles with wavecode simulations for (a) forward- and (b) reverse-impact experiments. The circles show the experimental data, and the solid lines are numerical simulations.

Lexan was treated as a hydrodynamic solid. In simulating the reverse-impact experiments, the material response of aluminum 6061 is important. Deviations for EPP behavior are well documented in aluminum.[32,33] The model used here incorporates anisotropic strain hardening[34] in addition to the parameters of Table II.

The final model for describing the dynamic response of 304 steel is compared to wave-profile measurements for selected forward- and reverse-impact experiments in Fig. 7. Significant improvements over the EPP model were achieved by incorporation of the Bauschinger effect and strain-rate dependent stress relaxation. Inclusion of stress relaxation improved the fit to the data at late times in the unloading history. A time constant of 15 ns was found to give the best fit to the unloading profiles. The incorporation of stress relaxation broadens the shock front to a much greater extent than was experimentally observed for the forward-impact experiments. The Bauschinger effect is responsible for smoothing the transition from elastic to plastic unloading. The Bauschinger model parameters are listed in Table X.

Release adiabats were calculated for the forward-impact experiments using a centered, simple-wave analysis[35]. The initial unloading point was first identified and connected to the Hugoniot state, using the EOS of the sample and window. The stress state at the sample-window interface was calculated from the nonlinear stress-particle velocity relationship for the window (Table II):

TABLE X. Parameters of Bauschinger model for the Fe–Cr–Ni alloy.

a_i	Y_i (GPa)
0.4	0.20
0.2	0.35
0.1	0.50
0.1	0.65
0.2	1.25

$$\sigma_w = \rho_0 c_0 u_w + \rho_0 s u_w^2, \tag{25}$$

where σ_w and u_w are the stress and particle velocity at the interface. The Lagrangian wave speed as a function of particle velocity, $c(u)$, was then estimated from release wave arrival times and the travel time of the shock (symmetric impact) or the travel time of the shock and release (nonsymmetric impact) through the flyer. An approximate correction was made for the effect of wave interactions near the window, based on the explicit analysis of the preceding section. The wave profiles were then corrected from interface to in-material conditions using the incremental expressions[36]:

$$du_s = \tfrac{1}{2}[du_w + d\sigma_w/\rho_0 c(u_s)], \tag{26}$$

$$d\sigma_s = \tfrac{1}{2}[d\sigma_w + \rho_0 c(u_s) du_w], \tag{27}$$

where σ_s and u_s are the in-material stress and particle velocity, respectively. Once the in-material properties are in hand, the conservation equations can be applied:

$$d\sigma_s = \rho_0 c(u_s) du_s, \tag{28}$$

$$d\eta = du_s/c(u_s), \tag{29}$$

to determine the stress-strain paths. Here the strain, η, is defined as

$$\eta = 1 - \rho_0/\rho. \tag{30}$$

A plot of Lagrangian wave speed, $c(u_s)$, versus strain is shown in Fig. 8. A gradual transition from elastic to plastic unloading behavior is evident. The Lagrangian bulk velocity at the Hugoniot state is estimated by extrapolating the linear plastic velocity trend to Hugoniot conditions[33]. The Eulerian bulk velocities are then obtained from Eq. (7) (Table VIII)

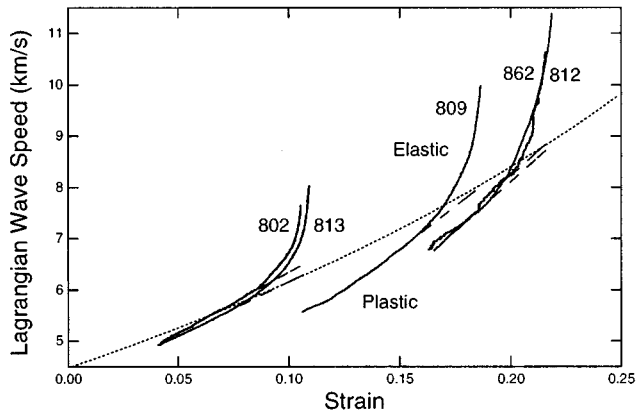

FIG. 8. Lagrangian wave speed in the Fe–Cr–Ni alloy as a function of strain determined from the centered, simple-wave analysis. The dashed lines are extrapolations of the bulk sound velocity to the Hugoniot state. The dotted curve is the Lagrangian bulk sound speed-strain relationship along the principal isentrope from extrapolation of ultrasonic data.

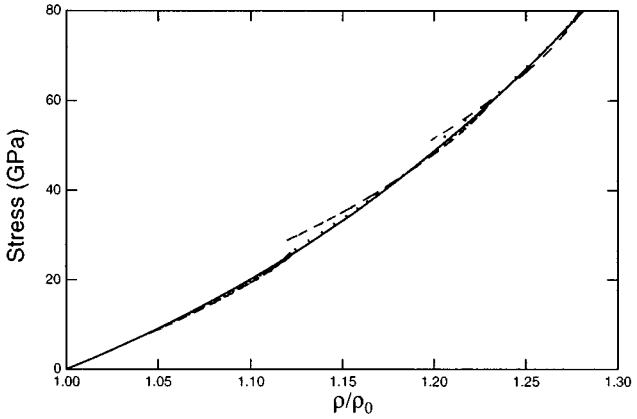

FIG. 9. Release adiabats from Fe–Cr–Ni alloy at three different stress levels. Dotted lines are calculated from simple-wave analysis. The dashed lines are inferred from wavecode simulations using the Mie–Grüneisen theory. The solid line is the principal Hugoniot.

The calculated release adiabats are shown in Fig. 9. Also shown are release adiabats extracted from the WONDY fits to the data. The wavecode uses the Mie–Grüneisen equation and the assumption that $\rho\gamma = \text{const}$, where γ is the Grüneisen constant. The release adiabats are initially steeper than the Hugoniot, reflecting the initial elastic response, but gradually become less steep. This is also illustrated in Fig. 10 where the stress differences between the Hugoniot and the release curves are plotted against density.

According to Fig. 9 and 10, the calculated release curve is less steep than the Mie-Grüneisen prediction at low densities for the higher stress experiments. There are two possible causes for this. First, the centered, simple-wave analysis strictly applies only to rate independent materials for which wave speed is constant at a given u. The computer simulations require some rate dependence to fit the profiles at late times. Second, the higher stress experiments used Ta

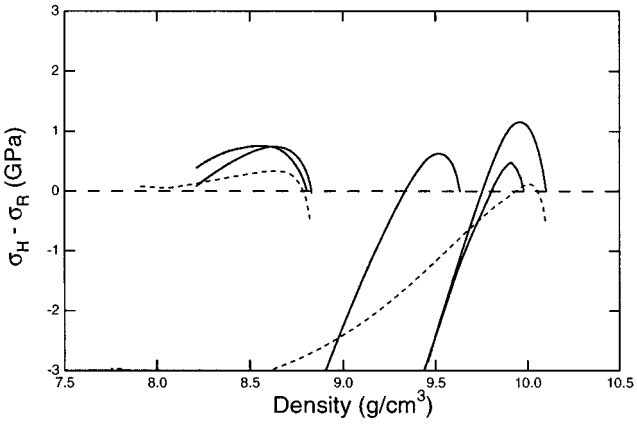

FIG. 10. Stress difference between the Hugoniot and release adiabat as a function of density for forward impact experiments (solid lines). A positive stress difference indicates that the release curve lies below the Hugoniot. σ_H is the Hugoniot stress and σ_R is the stress along the release adiabat. The dashed curves are taken from WONDY fits to representative high and low pressure wave profiles.

impactors, and the dispersion of the unloading wave through Ta has been neglected. This will lead to increasingly underestimated unloading wave speeds and hence calculation of a shallower release curve than actually occurs. In Fig. 10, the stress difference is initially negative for the WONDY results because of the effect of deviatoric stresses. The uncertainty in the Hugoniot states determined from impedance matching was ± 0.4 to ± 1.6 GPa for these experiments.

Returning to Fig. 8, the release wave speeds can be used to estimate the shear stress increase upon unloading following the method described in Ref. 33. The stress state in the shocked state can be written:

$$\sigma = P + \tfrac{4}{3}\tau, \tag{31}$$

where τ is the shear stress. The shear stress at the Hugoniot state is designated τ_0. For an EPP solid, this is equal to the maximum shear strength τ_c, which is also equal to $Y_0/2$. In real materials, τ_0 can be either above or below τ_c if hardening or softening has taken place. Upon unloading, τ decreases from τ_0 to a minimum value of $-\tau_c$ at the point at which reverse yielding occurs. Differentiation of the above equation with respect to engineering strain, η, yields

$$\frac{d\sigma}{d\eta} = \frac{dP}{d\eta} + \frac{4}{3}\frac{d\tau}{d\eta}, \tag{32}$$

which upon integration over strain from the Hugoniot state to the reverse yield point gives the following expression for the sum of the shear stress at the Hugoniot state and the shear strength maximum at reverse yielding

$$\tau_0 + \tau_c = \frac{3}{4}\rho_0 \int_{\eta_0}^{\eta_p} (V_P^2 - V_B^2)\, d\eta. \tag{33}$$

The difference $\tau_0 - \tau_c$ can be obtained from reloading experiments, and hence the components τ_0 and τ_c can be determined.[33] Since no reloading experiments were performed in the present study, only the sum can be determined. $\tau_0 + \tau_c$ is the shear stress change upon unloading. For the EPP model, the shear stress change is $2\tau_c$. The Lagrangian wave velocities required in the above equation were taken from the data of Fig. 8. The reverse yielding point is taken to be the strain at which the linear trend of the bulk velocities diverges from the measured wave speeds. The assumptions that are necessary in applying this technique are discussed in detail in Ref. 33. The shear stress changes for stainless steel 304 determined using the data of Fig. 8 are shown in Fig. 11. The stress dependence of $\tau_0 + \tau_c$ can be written as

$$\tau_0 + \tau_c = 0.149 + 0.018\sigma, \tag{34}$$

where σ is expressed in GPa.

The increase in $\tau_0 + \tau_c$ for 304 steel is similar to that observed in copper, where the shear stress change upon unloading increases from its ambient value 0.08 GPa to 1.5 GPa at 93 GPa.[37] Reference 20 summarizes data that also show shear strength increases in 2024 Al, 6061 Al, pure Al, Ta, Be, and W. For the aluminum data, a maximum in shear strength followed by a gradual decline is observed to occur. This is believed to be due to the shock-induced temperature rise. No strength maximum can be unequivocally identified

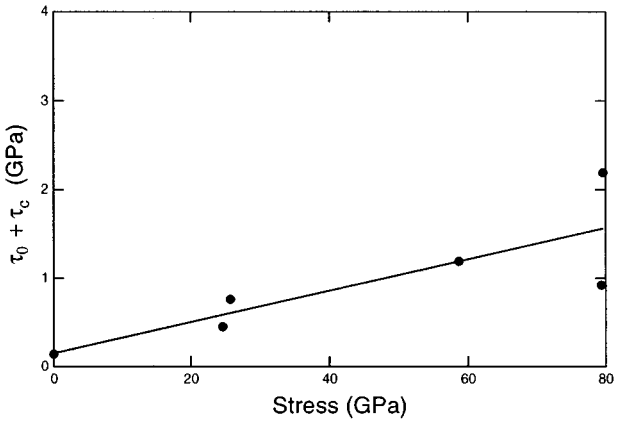

FIG. 11. Shear stress change upon unloading as a function of stress. The dashed line is a least-squares fit to the data.

for 304 steel over the range of the present data. The strength determinations near 80 GPa are divergent because of the large differences in unloading wave velocity inferred from the two experiments near this stress.

V. SUMMARY

Shock compression of the Fe–Cr–Ni alloy (304 stainless steel) was carried out to 80 GPa. Wave profiles were measured using interferometric techniques providing information on unloading wave velocities and high-strain-rate constitutive response.

Measured bulk and compressional wave velocities are similar to extrapolations of ultrasonic data. Bulk wave velocities are consistent with a constant $\rho\gamma = 17$, and compressional velocities required an increase in Poisson's ratio with compression. Elastic coefficients were extracted from the measured velocities using fourth-order Eulerian finite strain theory and assuming that unloading wave velocities represent fully elastic behavior. The first and second pressure derivatives of the longitudinal modulus along the Hugoniot are 7.9(0.5) and $-0.16(0.06)$ GPa^{-1}, respectively. The corresponding values for the bulk modulus are 6.4(1.0) and $-0.17(0.08)$ GPa^{-1}, respectively. The second pressure derivatives cannot be resolved from current ultrasonic data, but the values that result from truncation of the finite-strain expressions at third order in strain are $(\partial^2 C_L/\partial P^2)_S = -0.12$ GPa^{-1} and $(\partial^2 K_S/\partial P^2)_S = -0.08$ GPa^{-1}.

The Hugoniot elastic limit stress for 304 steel was found to be 0.35 GPa, implying a yield stress of 0.21 GPa. Computer simulations of measured wave profiles indicate substantial deviations from elastic perfectly-plastic response. The wave profiles were successfully reproduced by a constitutive model including anisotropic strain hardening (Bauschinger effect) and strain-rate-dependent stress relaxation.

A centered wave analysis was used to extract stress-strain histories from a subset of the experiments. Calculated release adiabats are initially steeper than the Hugoniot because of elastic response. The release adiabats show deviations from wavecode predictions that use the Mie–Grüneisen equation. The yield strength of 304 steel was found to in-

crease by at least a factor of 5 up to 80 GPa. Material strength is a small (2%–3%) but not negligible contributor to the total stress between 25 and 80 GPa.

ACKNOWLEDGMENTS

The authors thank M. Long, E. Gelle, A. Devora, K. Gallagher, and A. Campbell for experimental assistance. We also acknowledge L. Barker, O. B. Crump, and R. G. McQueen for helpful discussions. This research was supported by the National Science Foundation, Division of Geological and Planetary Sciences, California Institute of Technology Contribution No. 5806.

[1] R. G. McQueen, S. P. Marsh, J. W. Taylor, J. N. Fritz, and W. J. Carter, in *High-Velocity Impact Phenomena*, edited by R. Kinslow (Academic, New York, 1970), p. 294.
[2] J. D. Bass, T. J. Ahrens, J. R. Abelson, and T. Hua, J. Geophys. Res. **95**, 21 767 (1990).
[3] K. G. Gallagher, J. D. Bass, T. J. Ahrens, M. Fitzner, and J. R. Abelson, in *High-Pressure Science and Technology — 1993*, edited by S. C. Schmidt, J. W. Shaner, G. A. Samara, and M. Ross (AIP, New York, 1994), p. 963.
[4] H. M. Ledbetter, N. V. Frederick, and M. W. Austin, J. Appl. Phys. **46**, 3855 (1975).
[5] T. J. Ahrens, J. H. Lower, and P. L. Lagus, J. Geophys. Res. **76**, 514 (1971).
[6] T. J. Ahrens, in *Methods of Experimental Physics*, edited by C. G. Sammis and T. L. Henyey (Academic, San Diego, CA, 1987), Vol. 24, p. 185.
[7] S. P. Marsh, *LASL Shock Hugoniot Data* (University of California Press, Berkeley, CA, 1980).
[8] A. C. Mitchell and W. J. Nellis, J. Appl. Phys. **52**, 3363 (1981).
[9] L. M. Barker and R. E. Hollenbach, J. Appl. Phys. **41**, 4208 (1970).
[10] D. E. Grady and M. D. Furnish, Sandia Natl. Lab., Rep. SAND88-1642, Albuquerque, NM, 1988.
[11] L. M. Barker, in *Behavior of Dense Media under High Dynamic Pressure* (Gordon and Breach, New York, 1968), p. 483.
[12] L. M. Barker and R. E. Hollenbach, J. Appl. Phys. **43**, 4669 (1972).
[13] W. F. Hemsing, Rev. Sci. Instrum. **50**, 73 (1979).
[14] J. L. Wise and L. C. Chhabildas, in *Shock Waves in Condensed Matter—1985*, edited by Y. M. Gupta (Plenum, New York, 1986), p. 441.
[15] Ya. B. Zel'dovich and Y. P. Raizer, *Physics of Shock Waves and High-Temperature Hydrodynamic Phenomena* (Academic, New York, 1967).
[16] J. M. Walsh, M. H. Rice, R. G. McQueen, and F. L. Yarger, Phys. Rev. **108**, 196 (1957).
[17] T. S. Duffy and T. J. Ahrens, J. Geophys. Res. **100**, 529 (1995).
[18] J. Lipkin and J. R. Asay, J. Appl. Phys. **48**, 182 (1977).
[19] J. M. Brown and J. W. Shaner, in *Shock Waves in Condensed Matter—1983*, edited by J. R. Asay, R. A. Graham, and G. K. Straub (Elsevier, New York, 1984), p. 91.
[20] J. R. Asay and G. I. Kerley, Int. J. Impact Eng. **5**, 69 (1987).
[21] K. W. Schuler and J. W. Nunziato, Rheol. Acta **13**, 265 (1974).
[22] T. S. Duffy and T. J. Ahrens, J. Geophys. Res. **97**, 4503 (1992).
[23] J. N. Johnson, R. S. Hixson, G. T. Gray, and C. E. Morris, J. Appl. Phys. **72**, 429 (1992).
[24] D. Gerlich and S. Hart, J. Appl. Phys. **55**, 88 (1984).
[25] F. Birch, J. Geophys. Res. **83**, 1257 (1978).
[26] H. M. Ledbetter, W. F. Weston, and E. R. Naimon, J. Appl. Phys. **46**, 385 (1975).
[27] R. S. Hixson, R. G. McQueen, and J. N. Fritz, in *High-Pressure Science and Technology — 1993*, edited by S. C. Schmidt, J. W. Shaner, G. A. Samara, and M. Ross (AIP, New York, 1994), p. 105.
[28] E. Zaretsky and M. Kaluzhny, in *Shock Compression of Condensed Matter —1995*, edited by S. C. Schmidt and W. C. Tao (AIP, New York, 1996), p. 627.
[29] O. E. Jones and R. A. Graham, in *Accurate Characterization of the High-Pressure Environment*, edited by E. C. Boyd, NBS special pub. No. 326 (NBS, Washington, D.C., 1971), p. 229.
[30] C. E. Morris, *Los Alamos Shock Wave Profile Data* (University of California Press, Berkeley, CA, 1982).
[31] M. E. Kipp and R. J. Lawrence, Sandia Natl. Lab., Rep. SAND81-0930, Albuquerque, NM, 1982.
[32] W. Herrmann, Sandia National Lab. Report No. SLA-730897, Albuquerque, NM, 1974.
[33] J. R. Asay and L. C. Chhabildas, in *Shock Waves and High Strain-Rate Phenomena in Metals*, edited by M. A. Meyers and L. E. Murr (Plenum, New York, 1981), p. 417.
[34] R. J. Lawrence and J. R. Asay, in *High-Pressure Science and Technology*, edited by K. D. Timmerhaus and M. S. Barber (Plenum, New York, 1979), Vol. 1, p. 88.
[35] D. E. Grady, in *High-Pressure Research: Applications to Geophysics*, edited by M. H. Manghnani and S. Akimoto (Academic, New York, 1977), p. 389.
[36] J. R. Asay, L. C. Chhabildas, and D. P. Dandekar, J. Appl. Phys. **51**, 4774 (1980).
[37] L. C. Chhabildas and J. R. Asay, in *High Pressure in Research and Industry*, edited by C.-M. Backman, T. Johannisson, and L. Tegner, 8th AIRAPT Conference, 1982 (Arkitektkopia, Uppsala, Sweden, 1982), p. 183.